

# Self-assembled hole-selective contact for efficient Sn-Pb perovskite solar cells and all-perovskite tandems

Received: 20 August 2024

Accepted: 11 December 2024

Published online: 02 January 2025

Check for updates

Jingwei Zhu<sup>1,7</sup>, Xiaozhen Huang<sup>2,7</sup>, Yi Luo<sup>1</sup>, Wenbo Jiao<sup>1</sup>, Yuliang Xu<sup>1</sup>, Juncheng Wang<sup>1</sup>, Zhiyu Gao<sup>1</sup>, Kun Wei<sup>3</sup>, Tianshu Ma<sup>4,5</sup>, Jiayu You<sup>1</sup>, Jialun Jin<sup>1</sup>, Shenghan Wu<sup>1</sup>, Zhihao Zhang<sup>1</sup>, Wenqing Liang<sup>1</sup>, Yang Wang<sup>2,6</sup>✉, Shengqiang Ren<sup>1</sup>, Changlei Wang<sup>1</sup>✉<sup>4,5</sup>, Cong Chen<sup>1</sup>✉, Jinbao Zhang<sup>3</sup>✉ & Dewei Zhao<sup>1</sup>✉

Self-assembled monolayers (SAMs) have displayed unpredictable potential in efficient perovskite solar cells (PSCs). Yet most of SAMs are largely suitable for pure Pb-based devices, precisely developing promising hole-selective contacts (HSCs) for Sn-based PSCs and exploring the underlying general mechanism are fundamentally desired. Here, based on the prototypical donor-acceptor SAM MPA-BT-BA (BT), oligoether side chains with different length (i.e., methoxy, 2-methoxyethoxy, 2-(2-methoxyethoxy)ethoxy group) were custom-introduced on the benzothiadiazole unit to produce the target SAMs with acronyms MPA-MBT-BA (MBT), MPA-EBT-BA (EBT), and MPA-MEBT-BA (MEBT), respectively, and acting as HSCs for efficient Sn-Pb PSCs and all-perovskite tandems. The introduction of oligoether side chains enables HSCs effectively accelerate hole extraction, regulate the crystal growth and passivate surface defects of Sn-Pb perovskites. In particular, benefiting from the enhanced Sn-Pb perovskite film quality and the suppressed interfacial non-radiative recombination losses, EBT-tailored LBG devices yield a champion efficiency of 23.54%, enabling 28.61% efficient monolithic all-perovskite tandems with an impressive  $V_{OC}$  of 2.155 V and excellent operational stability as well as 28.22%-efficiency 4-T tandems.

Power conversion efficiency (PCE) of single-junction perovskite solar cells (PSCs) has been boosted to a certified 26.7%<sup>1</sup>. However, their theoretical efficiency has been invariably limited by Shockley-Queisser (S-Q) efficiency. The win-win collaboration between 1.7 and 1.9 eV wide-bandgap (WBG) perovskite top subcells and 1.1–1.3 eV mixed tin-

lead (Sn-Pb) low-bandgap (LBG) perovskite bottom subcells to fabricate all-perovskite tandem solar cells (TSCs) holds great potential to break the S-Q limit<sup>2–4</sup>.

Complementary spectral absorption, simple and low-cost solution processing, and friendly energy consumption of perovskites make

<sup>1</sup>College of Materials Science and Engineering & Engineering Research Center of Alternative Energy Materials & Devices, Ministry of Education, Sichuan University, Chengdu, China. <sup>2</sup>Strait Institute of Flexible Electronics (SIFE, Future Technologies), Fujian Normal University and Strait Laboratory of Flexible Electronics (SLoFE), Fuzhou, China. <sup>3</sup>College of Materials, Xiamen University, Xiamen, China. <sup>4</sup>School of Optoelectronic Science and Engineering, Soochow University, Suzhou, China. <sup>5</sup>Key Lab of Modern Optical Technologies of Education Ministry of China, Soochow University, Suzhou, China. <sup>6</sup>State Key Laboratory of Structural Chemistry, Fujian Institute of Research on the Structure of Matter, Chinese Academy of Sciences, Fuzhou, Fujian, China. <sup>7</sup>These authors contributed equally: Jingwei Zhu, Xiaozhen Huang. ✉ e-mail: [ifewangy@fjnu.edu.cn](mailto:ifewangy@fjnu.edu.cn); [chen.cong@scu.edu.cn](mailto:chen.cong@scu.edu.cn); [jinbao.zhang@xmu.edu.cn](mailto:jinbao.zhang@xmu.edu.cn); [dewei.zhao@scu.edu.cn](mailto:dewei.zhao@scu.edu.cn); [dewei\\_zhao@hotmail.com](mailto:dewei_zhao@hotmail.com)

all-perovskite TSCs develop rapidly<sup>5–16</sup>. In 2015, Zhou et al. constructed monolithic all-perovskite TSCs, demonstrating the proof-of-concept success of all-perovskite tandems with bottom-up solution-processing<sup>17</sup>. Recently, the reported PCEs of all-perovskite TSCs have beyond 28%<sup>18–20</sup>, obviously surpassing the highest efficiency of single-junction PSCs.

Hole-selective contact (HSC) with minimized interfacial non-radiative losses is an essential element to target the optimal performance of PSCs. Recently, self-assembled molecules (SAMs) have been displaying great potential as HSCs in perovskite-based devices<sup>21–30</sup>. The SAMs possess unique properties, such as simple preparation process, low synthesis cost, nearly negligible parasitic absorption, tunable energy levels, defect passivation ability, etc, offering viable promises to fabricate efficient solar cells<sup>31,32</sup>.

Though most of SAMs are suitable for pure-Pb WBG devices<sup>21,26,31–39</sup>, detailed studies on SAMs in Sn-based PSCs are still lacking, in which the acidic nature and parasitic absorption losses of widely-used PEDOT:PSS may limit the performance and stability of Sn-based PSCs<sup>40–47</sup>. This suggests that designing effective HSCs suitable for Sn-based devices is more challenging compared to their pure-Pb counterparts.

Notably, the energy levels of all the reported SAMs in Sn-Pb devices are mismatched with the corresponding perovskite layers compared to PEDOT:PSS<sup>48–51</sup>. Regulating Sn-Pb perovskite growth and achieving high-quality films with few defects on buried interface are critical requirements for the design of efficient HSCs in Sn-Pb PSCs<sup>52–54</sup>. Given that most SAMs reported to date are dominated by carbazole and its derivatives as building block which may be generally limited by few functional sites and uncontrollable electrical properties, donor-acceptor (D-A) SAMs established by our group show specific merits such as multifunctional sites, high dipole moment and tunable optoelectronic and interfacial properties<sup>34,47,48,55,56</sup>. In our previous work, the D-A SAM MPA-BT-BA (denoted as BT) has been proven to be effective as HSC in conventional PSCs<sup>55,57</sup>, however, it is not working well in Sn-Pb devices mainly due to the deficient regulation of Sn-Pb perovskites. Therefore, it is imperative to explore efficient SAMs with suitable dipole moment and excellent electrical properties so as to strengthen the properties of SAMs/perovskite interface and regulate the growth of Sn-Pb perovskites.

By leveraging the advantages of D-A backbone of SAMs, here we precisely designed a series of D-A type SAMs by incorporating oligoether side chain modulation strategy which can act as efficient HSCs for 1.25 eV  $\text{FA}_{0.6}\text{MA}_{0.3}\text{Cs}_{0.1}\text{Pb}_{0.5}\text{Sn}_{0.5}\text{I}_3$  PSCs and all-perovskite tandems. Generally, oligoether side chain engineering is adopted as an efficient chemical strategy to regulate the solubility, dipole moment, molecular stacking mode and the resultant electronic and interfacial properties of the organic semiconductors in the film state. In PSCs, oligoether side chain engineering can also endow HSCs with multifunctional properties either for small molecules<sup>38,59</sup>, metal complexes<sup>60</sup> or polymers<sup>61</sup>.

In this work, based on the prototypical D-A SAM, BT, oligoether side chains with different length (i.e., methoxy, 2-methoxyethoxy, 2-(2-methoxyethoxy)ethoxy group) were introduced on the benzothiadiazole unit to produce the target SAMs with acronyms MPA-MBT-BA (MBT), MPA-EBT-BA (EBT), and MPA-MEBT-BA (MEBT), respectively. As confirmed in the literatures that the introduction of oligoether chains at the 5,6-positions of benzothiadiazole unit can regulate the molecular packing and film morphological properties of the target molecules while maintaining their specific optoelectronic properties. While in this work, it was found that although the introduction of oligoether side chains elevated the energy level compared to BT, all the MBT, EBT, and MEBT can effectively regulate the crystal growth and passivate surface defects of Sn-Pb perovskites. In particular, EBT can achieve a balance among the properties of accelerated hole extraction, effective regulation of Sn-Pb perovskite processing and strong defects

passivation effect, which contribute to high-quality Sn-Pb perovskite and superior buried interface properties for suppressing non-radiative recombination losses. As a result, EBT-tailored LBG PSCs yield a champion efficiency of 23.54%, enabling 28.61% efficient two-terminal (2-T) all-perovskite tandems with an impressive  $V_{\text{OC}}$  of 2.155 V and 28.22%-efficiency 4-T tandems.

## Results

### Interconnection mechanisms of hole-selective contacts

The designed SAMs featuring oligoether side chains were synthesized within four steps (Supplementary Fig. 1) in a moderate total yield (Supplementary Table 1) and low-cost evaluation (Supplementary Table 2). Methoxy group substituted SAM MBT (4-(7-(4-(bis(4-methoxyphenyl)amino)phenyl)-5,6-dimethoxybenzo[c][1,2,5]thiadiazol-4-yl)benzoic acid) was obtained from the 4,7-dibromo-5,6-dimethoxybenzo[c][1,2,5]thiadiazole as the starting material, while EBT (4-(7-(4-(bis(4-methoxyphenyl)amino)phenyl)-5,6-bis(2-methoxyethoxy)benzo[c][1,2,5]thiadiazol-4-yl)benzoic acid) and MEBT (4-(7-(4-(bis(4-methoxyphenyl)amino)phenyl)-5,6-bis(2-methoxyethoxy)benzo[c][1,2,5]thiadiazol-4-yl)benzoic acid) were synthesized using oligoether side chain substituted benzothiadiazole unit which was afforded by nucleophilic substitution with 4,7-dibromo-5,6-difluorobenzo[c][1,2,5]thiadiazole as the starting material. The molecular structures of MBT, EBT and MEBT were confirmed by <sup>1</sup>H NMR<sup>13</sup>C NMR, and HRMS characterizations (Fig. 1a, Supplementary Figs. 2–10).

Supplementary Fig. 11 shows the front and side views of the corresponding molecules. Clearly, the four SAMs have the similar molecular configurations, in which anchoring group is benzoic acid (BA), 4-methoxy-N-(4-methoxyphenyl)N-phenylaniline (MPA) and benzo[c][1,2,5]thiadiazole (BT) are served as donor and acceptor units, respectively. The introduction of oligoether side chain hardly affect the backbone structure of the SAMs. Despite, the side chain engineering may have significant implications on the electric properties and molecular stacking behaviors of the SAMs. As shown in Supplementary Fig. 12, all the modified molecules exhibit blue-shifted absorption compared to BT, suggesting the enlarged molecular bandgap. It is reasonable that the introduction of oligoether side chains may elevate the energy levels of the SAMs due to their electron-donating nature. As seen in Supplementary Fig. 13 and Supplementary Table 3, the elevation of the lowest unoccupied molecular orbitals is larger than that of the highest occupied molecular orbitals (HOMOs), leading to the increase in bandgap. Figure 1b shows the electrostatic surface potential and dipole moment of molecules, EBT has a highest dipole moment of 7.88 D compared to BT (7.41 D), MBT (6.78 D), and MEBT (6.55 D), suggesting that EBT may have more efficient charge extraction capability<sup>62,63</sup>.

To more directly explore the effect of side chain engineering on molecular stacking behavior onto ITO substrate, molecular dynamics simulations were employed to investigate the microstructure of different molecules near the confined ITO substrate from the atomic level (Fig. 1c, Supplementary Fig. 14, and Supplementary Note 1), the density and orientation distribution are depicted in Fig. 1d. In terms of the orientation of the C-N axis, the angle between C-N and Z axis of BT is approximately 90°, i.e., the molecular backbone is nearly parallel to ITO substrate. In addition, the angles between molecular backbone and ITO substrates are about 15° and 5° for MBT and EBT, respectively. However, the C-N angle distribution of the MEBT molecule is mainly at 80° and/or 30°, i.e., the angle between MEBT backbone and ITO substrates is about 10° and/or 60°, implying more disordered distribution. Thus, it can be seen that BT, MBT, and EBT display a face-on dominant orientation on ITO substrate for efficient hole hopping and transport between the perovskites, HSCs, and ITO<sup>64</sup>, meanwhile MEBT exhibits a relatively disordered orientation when deposited on ITO. The variation of orientation distribution between molecules is mainly ascribed to the introduction of oligoether side chain in BT, among which 2-(2-

methoxyethoxy)ethoxy group induced the relatively disordered orientation of MEBT after anchoring to ITO substrate.

The thickness of the ultrathin film of different HSCs can be estimated by X-ray reflectivity (XRR) measurements (Supplementary Fig. 15a and Supplementary Note 2). Combining with the calculated molecular lengths (Supplementary Fig. 15b), it can be deduced that all the HSCs on ITO were formed as a multilayer film rather than monolayer film. The unanchored molecules remained on top of anchored ones<sup>65</sup>, and the uniform surface potential of four ITO/SAMs films (Supplementary Fig. 16) indicates the homogeneous distribution of all the molecules on the surface of ITO<sup>66</sup>. Moreover, part of molecules are

not anchored to ITO, so that oligoether side chains on the benzothiadiazole unit of MBT, EBT, and MEBT may have more chance to interact with the LBG perovskites for more efficient surface defect passivation and regulation of perovskite grain growth. Benefiting from efficient donor-acceptor HSC and high-quality perovskite films induced by oligoether side chains, the excess molecules hardly hinder the charge transport at the HSC/perovskite interface. We speculate that the incorporation of oligoether side chain can alter the molecular stacking and arrangement of the SAMs in the film state. The ordered molecular orientation along with high dipole moment is favorable for hole extraction and transportation. Moreover, the multiple oxygen

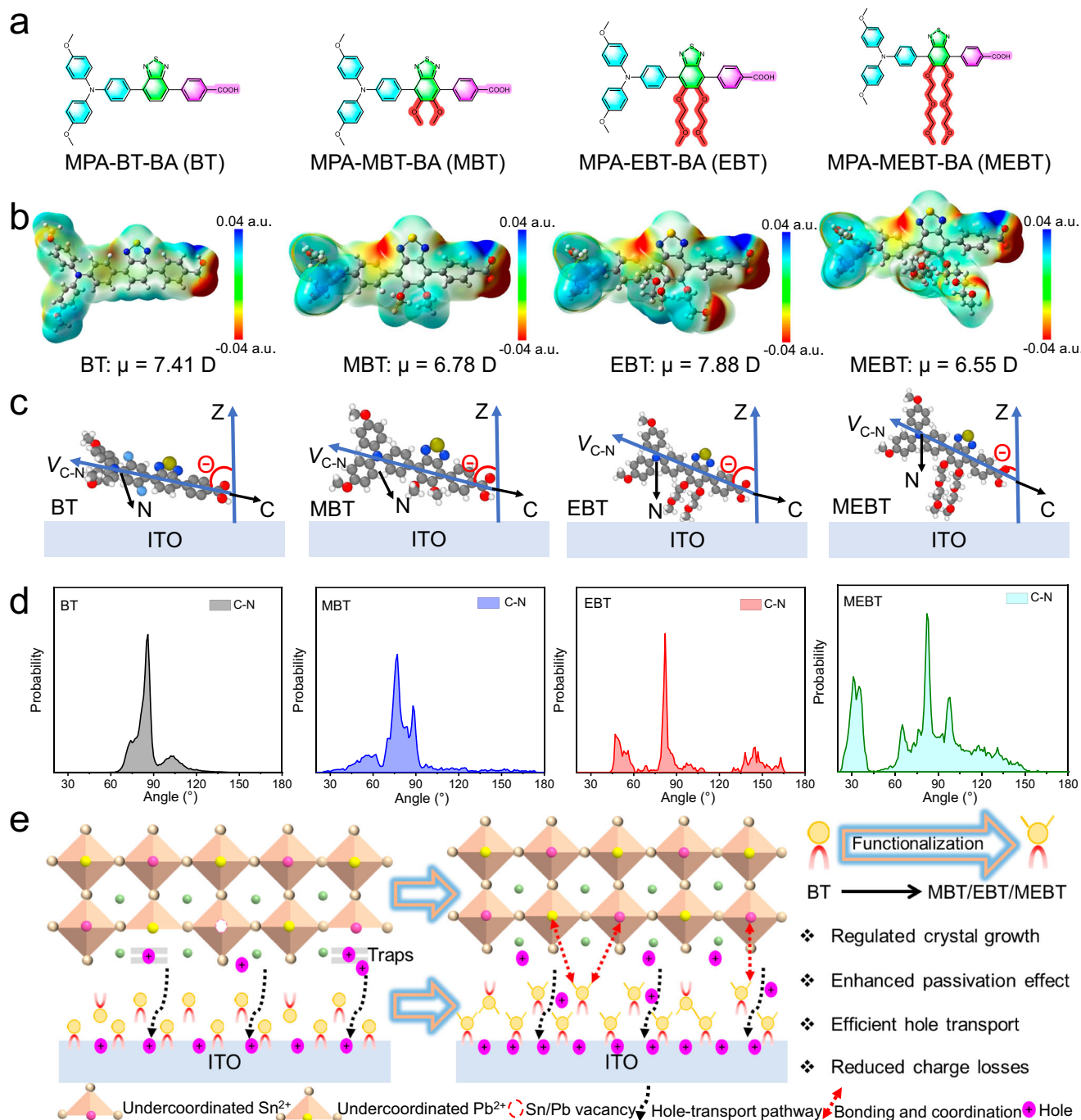


**Fig. 1 | Material properties and interconnection mechanism between ITO, HSCs, and perovskite. a** Molecular structure of BT, MBT, EBT, and MEBT. **b** Electrostatic surface potential and corresponding dipole moment of BT, MBT, EBT, and MEBT. Molecular dynamics simulation of hole-selective molecule on ITO

substrate. **c** Schematic of the C-N axis (i.e., the angle between the C-N and the Z-axis when the atom C points to the atom of BT, MBT, EBT, and MEBT). **d** Probability distribution of the C-N axis for BT, MBT, EBT, and MEBT. **e** Interconnection mechanisms between ITO, HSCs, and perovskite.

atoms on oligoether side chains can provide sufficient passivation sites toward defects of buried interface which may strengthen the passivation effect and reduce non-radiative recombination losses (Fig. 1e). The specific interaction mechanisms and the corresponding experimental analysis will be discussed as follow.

### Improved LBG Sn-Pb perovskite quality and underlying mechanism

Cyclic voltammetry (CV) was used to determine the energy levels of molecules as depicted in Supplementary Fig. 17 and Supplementary Table 1. We further detected the energy level alignment at the ITO/SAMs/LBG perovskite interfaces using ultraviolet photo-electron spectrometry (UPS) (Supplementary Fig. 18). As shown in Fig. 2a, the HOMO of ITO downshifts to  $-5.0$ – $-5.1$  eV after modification with SAMs, indicative of matched energy level with that of perovskite ( $-5.42$  eV). In addition, with the increase of oligoether side chain, the work functions (WFs) of modified ITO gradually upshifts from 4.14 eV (ITO/BT) to 4.10 eV (ITO/MBT), 3.98 eV (ITO/EBT) and 3.87 eV (ITO/MEBT), which may be attributed to the various dipole moments and different molecular orientations of the SAMs. If judging from the energetic picture only, the higher conduction band minimum and the

deeper WF are energetically more hole-selective and preferable for hole extraction. However, in a practical sense, other factors may profoundly influence the interfacial charge dynamics such as surface roughness, loading density of SAMs, interfacial contact and even the growth of overlaying perovskite layer<sup>55,67,68</sup>.

Hence, we investigated the effect of HSCs on the growth dynamics and quality of 1.25 eV Sn-Pb perovskite on different ITO/HSCs substrates. Thereafter, LBG perovskites on BT, MBT, EBT, and MEBT are denoted as BT/LBG, MBT/LBG, EBT/LBG, and MEBT/LBG, respectively. All HSCs exhibit comparable surface roughness on ITO (Supplementary Fig. 19). Compared to ITO/BT sample (Supplementary Fig. 20), the contact angle of DMF on ITO/MBT, ITO/EBT, and ITO/MEBT substrates successively decrease, indicating that a better wettability of the perovskite precursor on modified HSCs and therefore resulting in a uniform coverage of the perovskites.

As expected, the perovskite films deposited on modified HSCs show enhanced crystallinity (Supplementary Fig. 21). Meaningfully, the perovskite films show similar cross-sectional morphology (Supplementary Fig. 22). However, the surface morphology of modified perovskite films looks slightly different from that of the BT/LBG film (Fig. 2b and Supplementary Fig. 23). We attribute this difference to the

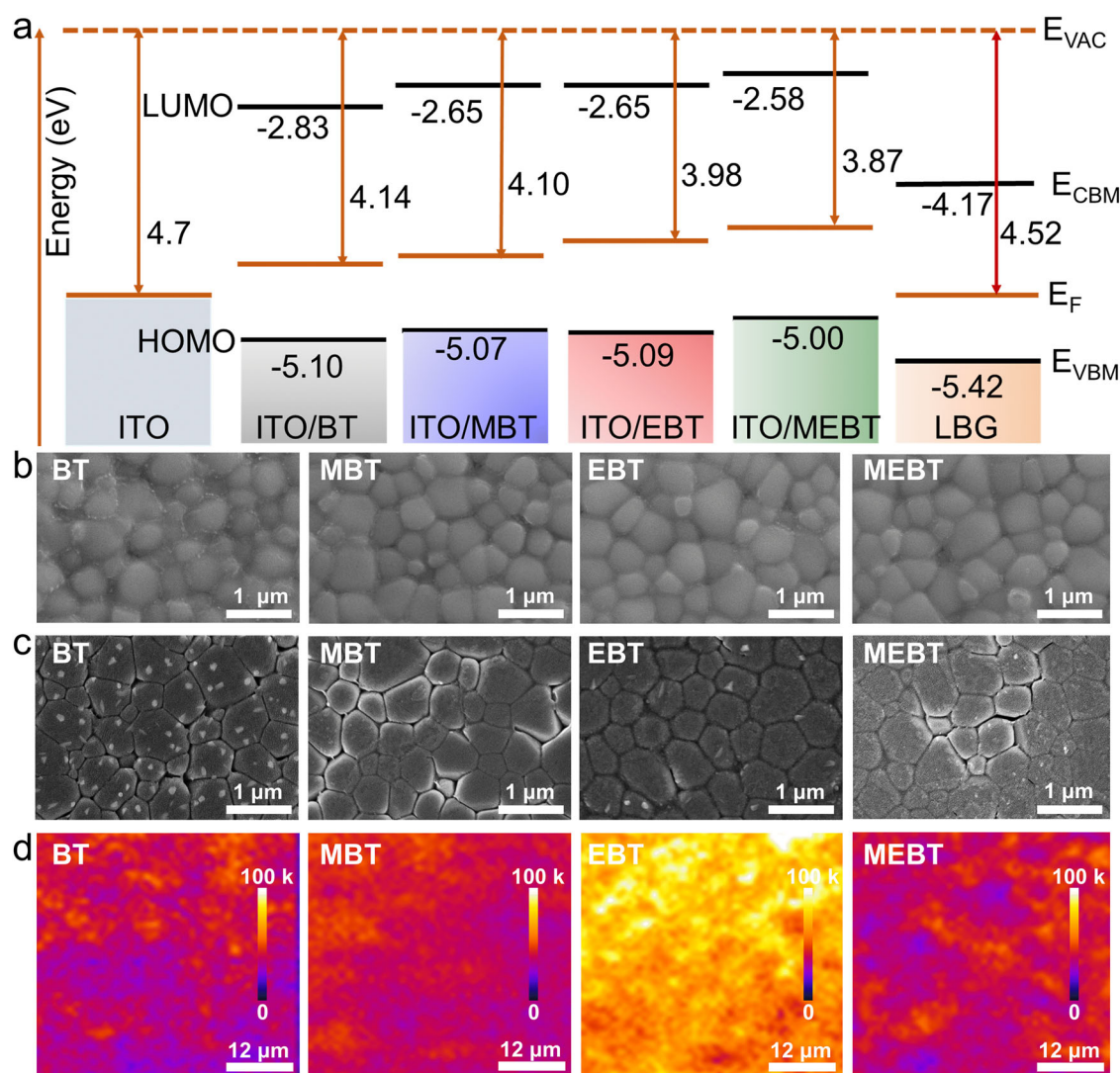


**Fig. 2 | Characterizations of improved Sn-Pb perovskite quality.** **a** Energy level diagrams of the HSCs/perovskite.  $E_F$  and  $E_{VAC}$  correspond to Fermi and vacuum levels, respectively.  $E_{CBM}$  and  $E_{VBM}$  correspond to the energy of the valence band maximum and conduction band minimum, respectively. **b** Top-view SEM images of

Sn-Pb perovskite films deposited on different HSCs. **c** SEM and **d** corresponding photoluminescence (PL) mapping images of buried interfaces of Sn-Pb perovskite films deposited on different HSCs.

effective oligoether side-chain engineering inducing the regulation of Sn-Pb perovskite crystallization. Moreover, their morphologies of buried surfaces are obviously different (Fig. 2c). The BT/LBG film exhibits disordered surface morphology with numerous small-size perovskite grains, meanwhile the density of PL mapping is lower and more inhomogeneous (Fig. 2d). After introducing side chains into BT, the EBT/LBG sample shows homogeneous surface morphology with compact and uniform perovskite grains, evidenced by the enhanced intensity and improved homogeneous PL mapping. The grain homogeneity of MEBT/LBG perovskite film gradually deteriorates and the corresponding PL mapping also exhibits weakened intensity and distribution uniformity, although their homogeneity is obviously better than that of BT/LBG sample. We attribute this to the relatively disordered orientation of MEBT after anchoring to ITO. The above phenomenon has indicated that the SAMs with distinct oligoether side chains could remarkably affect the growth process of Sn-Pb perovskites, especially the quality of buried surface of perovskite films.

Density functional theory (DFT) calculations (Supplementary Note 3) were performed to better reveal the underlying mechanism. Considering the processing conditions of perovskite films are very dynamic with variables, we calculated the binding energies of different oligoether groups with bare  $\text{Sn}^{2+}$  and  $\text{Pb}^{2+}$  ions (Fig. 3a). All the groups have a stronger coordination ability with  $\text{Sn}^{2+}$  compared to  $\text{Pb}^{2+}$  (Fig. 3b), suggesting that these groups would preferentially bind to Sn over Pb, which facilitates to regulate and retard the crystallization and growth process of Sn-contained perovskites, leading to balance of the crystallization of Sn- and Pb-contained perovskites. Henceforth,

compared to BT/LBG film, MBT/LBG, EBT/LBG, and MEBT/LBG films display more uniform perovskite grains (Fig. 2c).

We note that the coordination ability of oligoether side chains with  $\text{Sn}^{2+}$  depends on the chain length with an order of  $\text{MBT} < \text{EBT} < \text{MEBT}$ . As analyzed, the MEBT/LBG films should have the best uniform perovskite grains, but the opposite happened. This can be attributed to the relatively disordered orientation of MEBT and the formation of multilayer film after anchoring to ITO, largely making insufficient coordination between 2-(2-methoxyethoxy)ethoxy group with  $\text{Sn}^{2+}/\text{Pb}^{2+}$  ions. Thus, MEBT does not deliver the effective influence as MBT and EBT in regulating crystal growth of Sn-Pb perovskites, and the buried surface of MEBT/LBG film displays some small grains around mature grains (Fig. 2c). The further shift of Sn 3d and Pb 4f peaks for LBG/MBT, LBG/EBT, and LBG/MEBT films compared to that of LBG/BT sample in X-ray photoelectron spectroscopy (XPS) measurements (Supplementary Fig. 24) confirm the DFT calculations.

The surface potential of different perovskite films was also characterized with Kelvin probe force microscopy (KPFM). As shown in Fig. 3c, the lower and more uniform surface potential of EBT/LBG film indicates a lower WF and the decreased self p-doping<sup>69</sup> (i.e., reduced Sn vacancy density) induced by the oxidation of  $\text{Sn}^{2+}$  to  $\text{Sn}^{4+}$ , demonstrated by the reduced  $\text{Sn}^{4+}$  content in Fig. 3d. This means EBT not only regulates the growth process of Sn-Pb perovskite, but also improves the film quality making entire Sn-Pb perovskite crystal more stable overall for suppressing the oxidation of  $\text{Sn}^{2+11,70}$ .

Based on the above analysis, we can briefly summarize that EBT shows the face-on dominant orientation on ITO, higher dipole moment

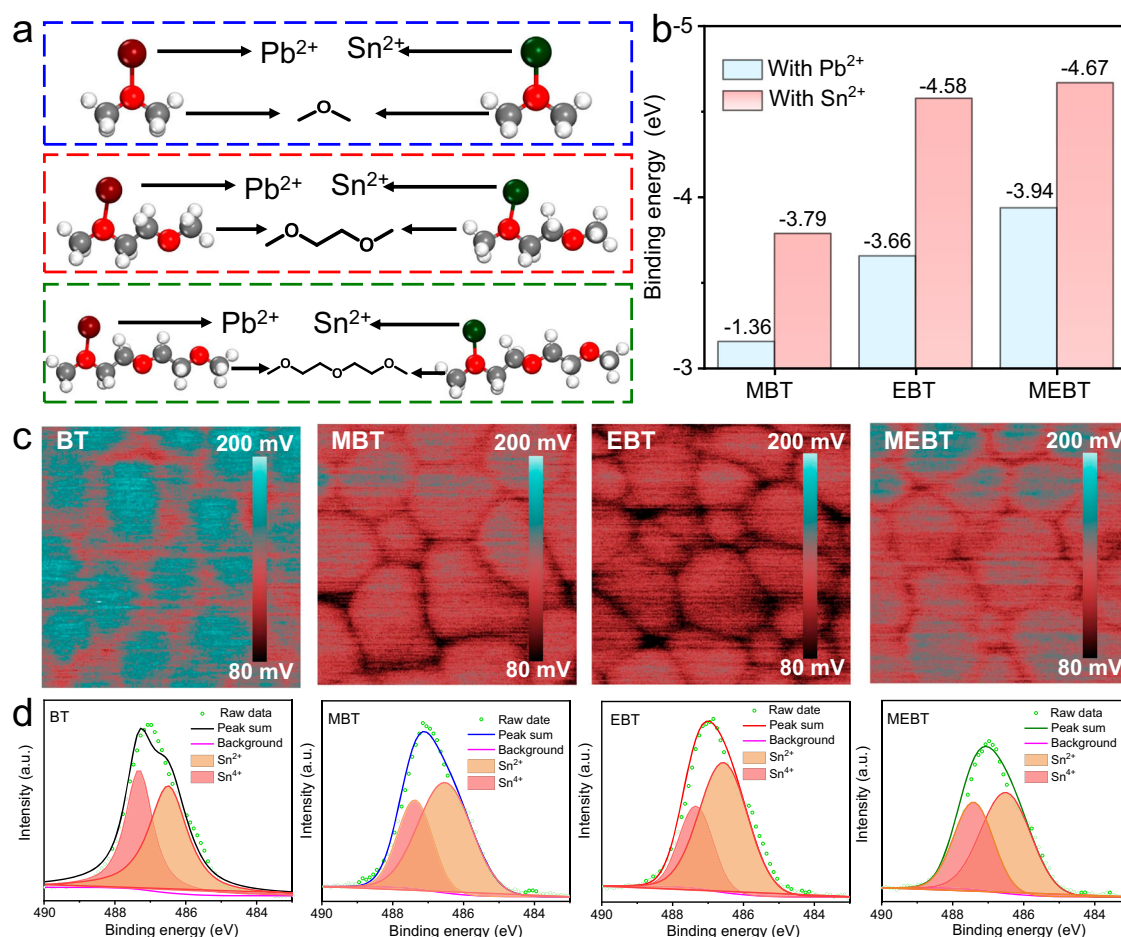


**Fig. 3 | DFT calculations and characterizations of LBG Sn-Pb perovskite films. a** Models of the interactions between MBT, EBT, and MEBT with  $\text{Pb}^{2+}$  and  $\text{Sn}^{2+}$  ions. **b** Interaction energies of MBT, EBT, and MEBT with  $\text{Pb}^{2+}$  and  $\text{Sn}^{2+}$  ions. **c** KPFM

images of Sn-Pb perovskite films deposited on different HSCs. The dimension of scanning area in KPFM images is  $2\ \mu\text{m}$  by  $2\ \mu\text{m}$ . **d** Sn 3d<sub>5/2</sub> XPS spectra of Sn-Pb perovskite films deposited on different HSCs.

for efficient charge extraction, efficient regulation of crystal growth and surface defect passivation for high-quality Sn-Pb perovskite films, beneficial for improved device performance.

### Performance of LBG Sn-Pb PSCs

We then fabricated 1.25 eV LBG PSCs with a structure of glass/ITO/HSCs/LBG perovskite/fullerene( $C_{60}$ )/2,9-dimethyl-4,7-diphenyl-1,10-phenanthroline (BCP)/Cu. As shown in Fig. 4a and Table 1, the BT/LBG PSC shows a PCE of 21.41 (21.04)% with an open-circuit voltage ( $V_{OC}$ ) of 0.854 (0.857) V, a short-circuit current density ( $J_{SC}$ ) of 32.51 (32.45)  $\text{mA cm}^{-2}$ , and a fill factor (FF) of 77.13 (75.67)% under reverse (forward) scan. Apparently, all the devices based on MBT, EBT, and MEBT yield enhanced photovoltaic performance. Especially the EBT/LBG PSC shows a champion PCE of 23.54 (23.49)% with a  $V_{OC}$  of 0.882 (0.880) V, a  $J_{SC}$  of 32.71 (32.75)  $\text{mA cm}^{-2}$ , and an FF of 81.59 (81.51)% under reverse (forward) scan. In addition, the EBT/LBG PSCs display lower hysteresis and better reproducibility (Supplementary Fig. 25). Notably, the performance of EBT/LBG PSCs displays a relatively wide window of suitable concentration processing of SAMs (at least between 0.3  $\text{mg mL}^{-1}$  and 0.5  $\text{mg mL}^{-1}$ , Supplementary Fig. 26), and then 0.35  $\text{mg mL}^{-1}$  is the optimal concentration for HSCs. This wide

processing window of solution concentration further demonstrates the promise of employing SAMs as HSCs for efficient perovskite-based devices.

The BT/LBG, MBT/LBG, EBT/LBG, and MEBT/LBG PSCs yield EQE-integrated  $J_{SC}$ s of 32.07, 32.20, 32.31, and 32.14  $\text{mA cm}^{-2}$  (Fig. 4b), respectively. All the ITO/SAMs samples yield excellent transparency due to their ultra-thin thickness (Supplementary Fig. 27), and so we can attribute the enhanced  $J_{SC}$ s of modified devices to the improved Sn-Pb perovskite quality. In addition, after replacing BT with EBT as HSC, the FF and  $V_{OC}$  of LBG PSCs show the more significant improvement. We attribute the enhanced FF to EBT-induced high-quality perovskite films, efficient hole transport for suppressing non-radiative recombination losses at the HSC/perovskite interface<sup>38</sup>.

Figures 4c, d show the steady-state PL spectra and time-resolved photoluminescence (TRPL) decays. The EBT/LBG sample has a higher PL intensity and longer carrier lifetime  $\tau_2$  (651.5 ns) than those of BT/LBG (212.1 ns), MBT/LBG (424.9 ns), and MEBT/LBG (247.4 ns), where the longer  $\tau_2$  is mainly ascribed to suppressed interfacial non-radiative recombination losses, which agrees well with the results of PL mapping images of buried interfaces of perovskite films (Fig. 2d).

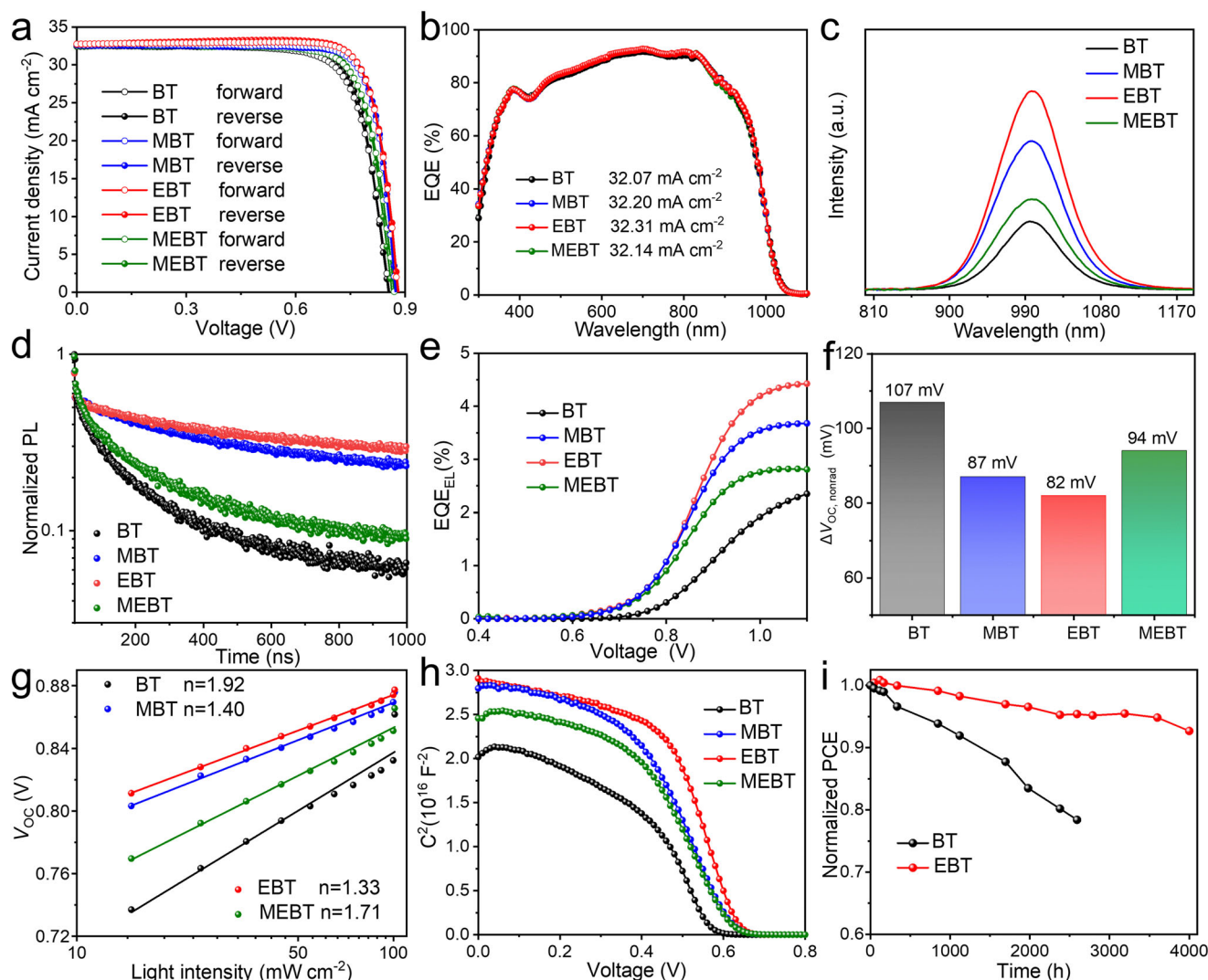


**Fig. 4 | Photovoltaic performance of single-junction Sn-Pb PSCs. a**  $J$ - $V$  curves and **b** External quantum efficiency (EQE) spectra of different LBG PSCs. **c** PL and **d** TRPL decays of LBG perovskites deposited on different ITO/HSCs substrates. **e** Voltage-dependent  $\text{EQE}_{EL}$  spectra and **f** the corresponding  $\Delta V_{OC, \text{nonrad}}$  of different LBG

PSCs. **g**  $V_{OC}$  dependence on light intensity and **h** Mott-Schottky plots of different LBG PSCs. **i** Long-term stability of different LBG PSCs at room temperature in  $N_2$  atmosphere. The initial PCEs of corresponding BT/LBG and EBT/LBG PSCs are 23.31% and 21.06%, respectively.

**Table 1 | Summary on photovoltaic performance of single-junction PSCs and all-perovskite tandems including 1.25 eV LBG PSCs, BT and EBT-tailored 2-T all-perovskite tandems under reverse and forward voltage scans, and 1.77 eV WBG top cell, filtered LBG bottom cell and corresponding 2-T all-perovskite tandems under reverse voltage scan**

| Cells        | HSC  | Scan direction | $V_{OC}$ (V) | $J_{SC}$ (mA cm <sup>-2</sup> ) | FF (%) | PCE (%) |
|--------------|------|----------------|--------------|---------------------------------|--------|---------|
| LBG          | BT   | Reverse        | 0.854        | 32.51                           | 77.13  | 21.41   |
|              |      | Forward        | 0.857        | 32.45                           | 75.67  | 21.04   |
|              | MBT  | Reverse        | 0.876        | 32.61                           | 80.98  | 23.13   |
|              |      | Forward        | 0.873        | 32.63                           | 80.95  | 23.06   |
|              | EBT  | Reverse        | 0.882        | 32.71                           | 81.59  | 23.54   |
|              |      | Forward        | 0.880        | 32.75                           | 81.51  | 23.49   |
|              | MEBT | Reverse        | 0.864        | 32.6                            | 78.6   | 22.13   |
|              |      | Forward        | 0.870        | 32.49                           | 77.88  | 22.01   |
| 2-T          | BT   | Reverse        | 2.121        | 15.93                           | 79.75  | 26.95   |
|              |      | Forward        | 2.116        | 15.96                           | 79.51  | 26.85   |
|              | EBT  | Reverse        | 2.155        | 16.05                           | 82.73  | 28.61   |
|              |      | Forward        | 2.153        | 16.08                           | 82.37  | 28.52   |
| WBG          | 2F   | Reverse        | 1.3          | 17.85                           | 82.39  | 19.12   |
| Filtered LBG | EBT  | Reverse        | 0.836        | 13.4                            | 81.23  | 9.1     |
| 4-T          | -    | Reverse        | -            | -                               | -      | 28.22   |

To further quantify the non-radiative recombination losses and explore the enhanced  $V_{OC}$ , EQE<sub>EL</sub> measurements were performed. Apparently, the higher EQE<sub>EL</sub> value of EBT/LBG PSCs (Fig. 4e) demonstrates the suppressed interfacial non-radiative recombination losses, agreeing with the larger recombination resistance in low-frequency region (Supplementary Fig. 28).  $V_{OC}$  losses caused by non-radiative recombination ( $\Delta V_{OC, nonrad}$ ) can be quantified with the formula:  $\Delta V_{OC, nonrad} = -\frac{k_B T}{q} \ln(EQE_{EL})^{71}$ , we then calculated the  $\Delta V_{OC, nonrad}$  values of different PSCs and depicted in Fig. 4f. The EBT/LBG PSCs yield a lower  $\Delta V_{OC, nonrad}$  value of 82 mV than those of BT/LBG (107 mV), MBT/LBG (87 mV), and MEBT/LBG (94 mV) devices, which is consistent with higher  $V_{OC}$  output of EBT/LBG PSCs. We also found that EBT/LBG PSCs exhibit smaller ideality factor (Fig. 4g) and larger built-in potential (Fig. 4h), further demonstrating the significantly suppressed nonradiative recombination losses and stronger driving force for higher  $V_{OC}$  output inside the devices.

The EBT-tailored LBG PSCs display superior long-term stability. As shown in Fig. 4i, the EBT/LBG PSCs can retain over 95% of their initial efficiency after storage of 3600 h in N<sub>2</sub> atmosphere, which is mainly ascribed to the improved Sn-Pb perovskite films quality and suppressed interfacial non-radiative losses.

### Performance of all-perovskite tandem solar cells

We then fabricated 2-T all-perovskite TSCs with the architecture of glass/ITO/2F/1.77 eV FA<sub>0.8</sub>CS<sub>0.2</sub>Pb(I<sub>0.6</sub>Br<sub>0.4</sub>)<sub>3</sub> WBG perovskite (1.2 M)/C<sub>60</sub>/ALD-SnO<sub>2</sub>/indium zinc oxide (IZO)/PEDOT:PSS/BT or EBT/1.25 eV LBG perovskite/C<sub>60</sub>/BCP/Cu. The 1.77 eV WBG PSC yields a PCE of 19.44 (19.41)% with a  $V_{OC}$  of 1.32 (1.32) V, a  $J_{SC}$  of 17.81 (17.81) mA cm<sup>-2</sup>, and an FF of 82.68 (82.58)% under reverse (forward) scan (Supplementary Fig. 29a). The corresponding EQE-integrated  $J_{SC}$  of 17.21 mA cm<sup>-2</sup> (Supplementary Fig. 29b), which is almost consistent with the  $J_{SC}$  obtained from  $J$ - $V$  curve. Figure 5a shows the cross-sectional SEM image of EBT-tailored all-perovskite tandem. As shown in Fig. 5b and Table 1, BT-tailored 2-T TSCs only show a PCE of 26.95 (26.85)% with a  $J_{SC}$  of 15.93 (15.96) mA cm<sup>-2</sup>, a  $V_{OC}$  of 2.121 (2.116) V, and an FF of 79.75 (79.51)% under reverse (forward) scan. The best-

performing EBT-tailored 2-T tandem yields a champion PCE of 28.61 (28.52)% with a  $J_{SC}$  of 16.05 (16.08) mA cm<sup>-2</sup>, a  $V_{OC}$  of 2.155 (2.153) V, and an FF of 82.73 (82.37)% under the reverse (forward) voltage scan. The integrated  $J_{SC}$ s of WBG and LBG subcells in EBT-tailored 2-T TSCs are 15.91 and 16.04 mA cm<sup>-2</sup>, respectively (Fig. 5c). Moreover, our optimized 2-T TSCs achieve an average PCE and  $V_{OC}$  of 28.13% (Fig. 5d) and 2.14 V (Fig. 5e), respectively.

We also investigated the operating stability of unencapsulated tandems under simulated 1-sun illumination with maximum power point (MPP) tracking in glovebox (Fig. 5f). Our EBT-tailored tandem shows excellent operational stability and can retain 92% of its initial efficiency after 400 h of continuous illumination.

To further demonstrate the potential of the EBT-tailored LBG PSCs in all-perovskite tandems, we fabricated 4-T all-perovskite TSCs by mechanically stacking 1.77 eV WBG perovskite (1.4 M) top subcells with our EBT/LBG perovskite bottom subcell (Supplementary Fig. 30). As shown in Fig. 5g, the semi-transparent WBG top subcell has a PCE of 19.12%, the EBT/LBG bottom subcell yields a PCE of 23.3% meanwhile its filtered PCE is 9.1%. The EQE-integrated  $J_{SC}$ s of semi-transparent WBG top subcell and filtered EBT/LBG bottom subcell are 17.5 and 13.0 mA cm<sup>-2</sup>, respectively (Fig. 5h). As a result, our champion 4-T tandem yields a PCE of 28.22%, which is among the highest reported values of 4-T all-perovskite TSCs.

## Discussion

We have demonstrated that oligoether side-chain engineering enables efficient donor-acceptor self-assembled HSCs for Sn-Pb LBG PSCs and all-perovskite tandems. Benefiting from the efficient charge extraction and EBT-induced high-quality Sn-Pb perovskite films by regulating the crystal growth and passivating surface defects, the interfacial non-radiative recombination losses are effectively reduced inside the EBT-tailored devices. As a result, EBT-tailored LBG PSCs achieve a champion PCE of 23.54%, enabling 28.61% efficient monolithic all-perovskite TSCs with an impressive  $V_{OC}$  of 2.155 V and excellent operational stability as well as 28.22%-efficiency 4-T tandems. This work provides an important insight into promising molecular design strategy to precisely explore charge-selective materials suitable for various-bandgap perovskites towards efficient perovskite-based single-junction and tandem devices.

## Methods

### Materials

The synthesis process of BT, MBT, EBT, and MEBT molecule was described in the synthesis section in Supplementary note 1. N,N-dimethylformamide (DMF, 99.8%), dimethyl sulfoxide (DMSO, 99.9%), chlorobenzene (CB, 99.9%), toluene (TL), isopropanol (IPA, 99.5%), tin (II) flourine (SnF<sub>2</sub>, 99%), tin (II) iodide (SnI<sub>2</sub>, 99.999%), tin (II) fluorine (SnF<sub>2</sub>, 99%), Pb(SCN)<sub>2</sub>, and ammonium thiocyanate (NH<sub>4</sub>SCN) were purchased from Sigma-Aldrich. Formamidinium iodide (FAI) and Methylammonium iodide (MAI) were purchased from Greatcell Solar Company. Lead bromide (PbBr<sub>2</sub>) and lead iodide (PbI<sub>2</sub>) were purchased from TCI. Cesium iodide (CsI, 99%) was purchased from Alfa Aesar. Diethyl ether (DE) was purchased from Chengdu Chron Chemical Co., Ltd. Ethylenediammonium diiodide (EDA<sub>2</sub>, 98%) was purchased from Xi'an Polymer Light Technology Corporation. C<sub>60</sub> was purchased from Nano-C. Copper (Cu) was purchased from Zhongnuoxincai Co., Ltd. Tetrakis(dimethylamino) tin (IV) (99.9999%) for ALD-SnO<sub>2</sub> was purchased from Nanjing Ai Mou Yuan Scientific Equipment Co., Ltd. The ceramic 2-inch indium zinc oxide (IZO) target was purchased from Shijiazhuang Huake metal material technology Co., Ltd.

### Precursor preparation

HSCs solution: HSCs solution was obtained by dissolving 0.35 mg of BT/MBT/EBT/MEBT in 1 mL of TL solution and stirred for 2 h.

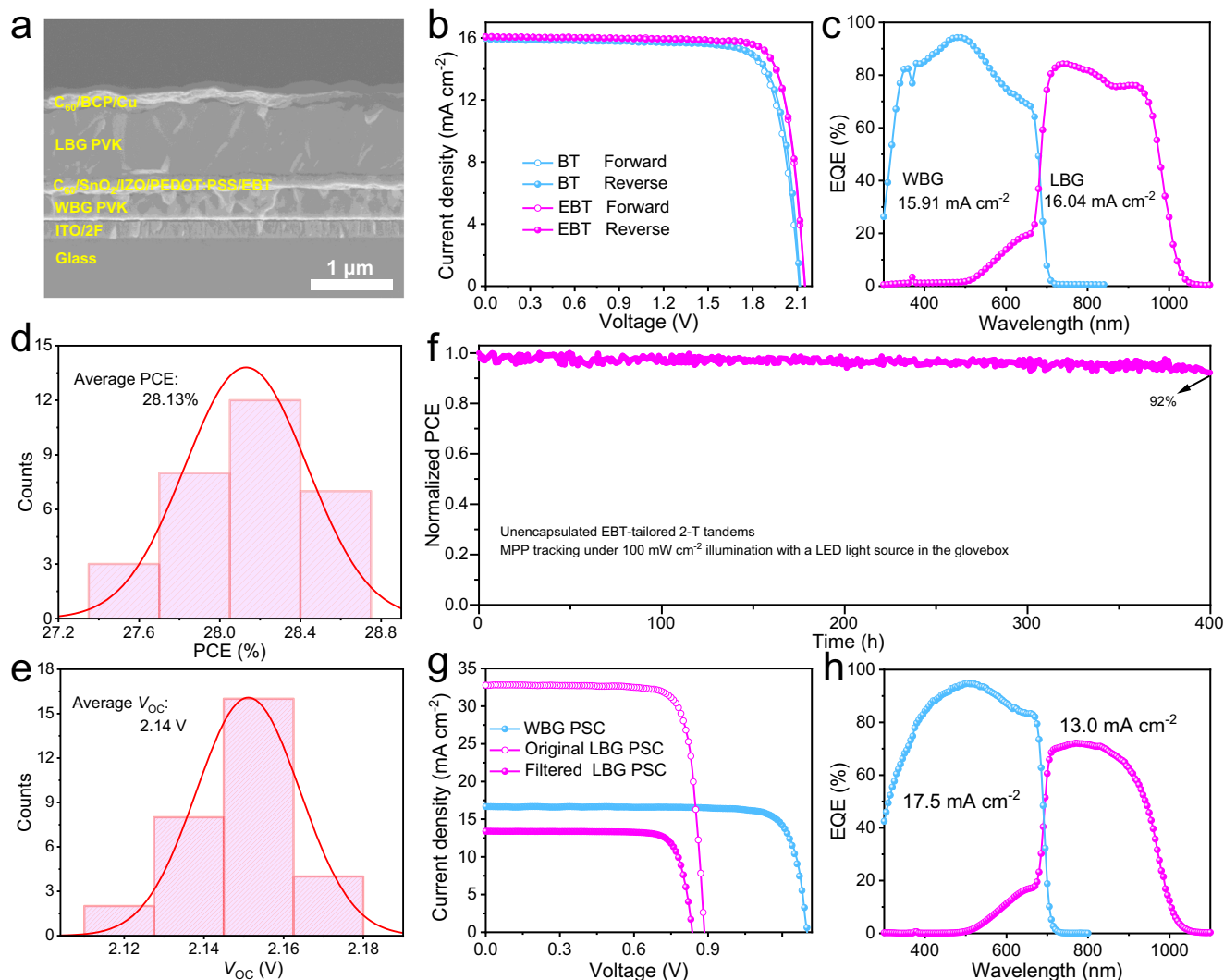


**Fig. 5 | Photovoltaic performance of all-perovskite tandems.** **a** Cross-sectional SEM image of an entire EBT-tailored all-perovskite TSC. **b**  $J$ - $V$  curves of BT and EBT-tailored all-perovskite tandems. **c** EQE spectra of subcells in the best-performing all-perovskite tandems. **d** PCE and **e**  $V_{OC}$  histograms of 30 EBT-tailored tandem cells. **f** MPP tracking of EBT-tailored 2-T all-perovskite TSC was performed using

multicolor LED solar simulator with AM1.5 G in a glovebox at about 25–30 °C. The initial PCE of corresponding all-perovskite tandem cell is 28.4%. **g**  $J$ - $V$  curves of WBG top cell, original LBG bottom cell, and filtered LBG bottom cell. **h** EQE spectra of WBG top cell and filtered LBG bottom cell.

1.25 eV LBG perovskite  $\text{FA}_{0.6}\text{MA}_{0.3}\text{Cs}_{0.1}\text{Pb}_{0.5}\text{Sn}_{0.5}\text{I}_3$ ; 1.8 M LBG precursor was obtained after dissolving 414.91 mg of  $\text{PbI}_2$ , 335.27 mg of  $\text{SnI}_2$ , 185.73 mg of FAI, 85.84 mg of MAI, 46.77 mg of CsI, 14.10 mg of  $\text{SnF}_2$ , and 2.57 mg of  $\text{NH}_4\text{SCN}$  in 1 mL mixed solution of DMF and DMSO (DMF: DMSO = 3:1, v:v). Then the precursor was stirred for 5 h and filtered through a 0.22  $\mu\text{m}$  PTFE filter before use.

1.77 eV WBG perovskite  $\text{FA}_{0.8}\text{Cs}_{0.2}\text{Pb}(\text{I}_{0.6}\text{Br}_{0.4})_3$ ; 1.2 M WBG precursor was prepared by dissolving the 0.96 mmol FAI, 0.24 mmol CsI, 0.48 mmol  $\text{PbI}_2$ , 0.72 mmol  $\text{PbBr}_2$  and 0.012 mmol  $\text{Pb}(\text{SCN})_2$  in 1 mL mixed solution (DMF:DMSO = 3:1, v:v) and stirred overnight. 1.4 M WBG precursor was prepared with the same way.

### Device fabrication

**1.25 eV LBG PSCs:** The cleaning of ITO substrates is the same as the previous work<sup>48</sup>. ITO substrates were cleaned with detergent, deionized water, and ethanol for 15 min in turn. The obtained substrates were dried with nitrogen flow and cleaned by ultraviolet-ozone for 15 min, and then moved them into a nitrogen-filled glovebox. For BT/MBT/EBT/MEBT HSCs, 60  $\mu\text{L}$  solution (0.35  $\text{mg mL}^{-1}$  in TL) was deposited on the ITO substrates and then spin-coated at 3000 rpm for

20 s, followed by annealing at 105 °C for 10 min. 55  $\mu\text{L}$  perovskite precursor solution was spin-coated onto the HSCs by a two-step process (1000 rpm for 10 s and 4000 rpm for 50 s). 500  $\mu\text{L}$  CB was dropped onto the substrates during the second spin-coating step. Then, the perovskite films were annealed at 100 °C for 10 min. 70  $\mu\text{L}$  EDAl<sub>2</sub> solution was deposited on the LBG perovskite films at 4000 rpm for 30 s, followed by annealing at 100 °C for 5 min. Finally, the obtained perovskite films were successively evaporated 20-nm  $\text{C}_{60}$ , 5-nm BCP and 100-nm Cu.

**All-perovskite TSCs:** The cleaning of ITO substrates is the same as mentioned above. 70  $\mu\text{L}$  solution (0.3  $\text{mg mL}^{-1}$ ) of 2F dissolved in TL was deposited on the ITO substrates and spin-coated at 4000 rpm for 30 s, followed by annealing at 100 °C for 15 min. The perovskite precursor was dropped on HSCs and immediately spin-coated using a two-stage technique (500 rpm for 2 s and 4000 rpm for 60 s), with 660  $\mu\text{L}$  DE dripped at 25 s of the second step. Then the obtained WBG perovskite films were annealed at 60 °C for 2 min, followed by 100 °C for 10 min. After the perovskite films were cooled down, 70  $\mu\text{L}$  of 2-thiopheneethylammonium chloride (TEACl) solution was deposited onto the perovskite films at 3000 rpm for 30 s, and annealed at 100 °C

for 5 min. The as-prepared perovskite films were transferred to an evaporation chamber and evaporated 20 nm- $C_{60}$ . Then the samples were transferred to the ALD chamber (Ensure scientific) to deposit 20 nm- $SnO_2$  film at 90 °C with tetrakis(dimethylamino)-tin(IV) (TDMA-Sn) as the Sn source and water as the oxidizer. 100-nm IZO was sputtered at a 70 W power during under Ar pressure of 0.3 Pa to obtain semi-transparent WBG subcells. For the 2-T all-perovskite tandems, PEDOT:PSS diluted with IPA (v:v = 1:4) was deposited onto the as-prepared IZO layer and then annealed at 100 °C for 5 min, and followed by depositing HSCs with annealing at 105 °C for 5 min. Last, the obtained films were transferred to glovebox for the fabrication of LBG subcells as mentioned above. Finally, the 2-T all-perovskite TSCs with a structure of glass/ITO/2F/WBG perovskite/ $C_{60}$ /ALD- $SnO_2$ /IZO/PEDOT:PSS/HSCs/LBG perovskite/ $C_{60}$ /BCP/Cu were fabricated.

### Characterizations of HSMs

$^1H$  NMR and  $^{13}C$  NMR spectra were performed on the Bruker Ascend 400 MHz spectrometer. ThermoScientific™ Q-Exactive was employed to perform high-resolution mass (HRMS) spectra. Elemental analyses (EAs) of compounds were characterized at Shenzhen University (Shenzhen, Guangdong, China). XRR curves were acquired on an X-ray diffractometer with a rotating Cu-K $\alpha$  anode source.

### Characterizations of films and devices

The top-view and cross-sectional SEM images of all the perovskite films and devices were performed with a field emission SEM instrument (Hitachi S-4800), and the top-view SEM images of buried surface were characterized with SEM (SU-70, Japan Hitachi Nake high-tech enterprise). PL intensity mapping of different perovskite films were performed by Vis-NIR-XU (Nanophoton Corporation) with an excitation of 532 nm. The exfoliation process of the Sn-Pb perovskite films is same as that of our previous work<sup>72</sup>. The exfoliation technique of perovskite buried interfaces via blade-coating a bilayer film composed of self-polymerized epoxy resin on the surface of perovskite film. Firstly, 50  $\mu$ L solution (0.4 mg mL<sup>-1</sup>) of PMMA dissolved in TL was blade-coated on the surface of perovskite film. Epoxy precursor was obtained by mixing diglycidyl ether bisphenol A type, n-octylamine and m-xylenediamine, and then the epoxy layer was blade-coated on the prepared perovskite film and annealed at 70 °C for 10 min. After the epoxy was completely solidified at room temperature, perovskite film can be easily exfoliated from ITO substrate with a glass nipping plier. AFM and KPFM images of different samples were obtained by a Bruker Nano Inc DI Multi Mode 8. For KPFM images, surface potential difference between the sample and tip is a relative value, which reflects the average SP distribution of the sample. X-ray diffractometer (Bruker D2 Phase) with Cu-K $\alpha$  radiation ( $\lambda = 0.154$  nm) was used to characterize XRD patterns of perovskite films under 30 kV and 10 mA excitation. The steady-state PL and TRPL measurements were measured by FLS980 (Edinburgh Inc.). PL spectra were obtained using a 532-nm Xe lamp with a monochromator. TRPL were characterized through a supercontinuum pulsed laser (Wuhan Yangtze Soton Laser Co. Ltd.) with a wavelength of 532 nm. UV-Vis optical absorption spectra were obtained by an ultraviolet-visible spectrophotometer (PerkinElmer Lambda 950). Ultraviolet photoemission spectroscopy (UPS) was characterized employing the photoelectron spectrometer (ESCALAB 250Xi, Thermo Fisher Scientific). XPS spectra of different perovskite films were performed with a photoelectron spectrometer (ESCALAB 250Xi, Thermo Fisher Scientific).

*J-V* curves of solar cells were obtained with Keysight B2901A source meter under AM1.5 G illumination using solar simulator (SS-F5, Enlitech) with an output intensity of 100 mW cm<sup>-2</sup> in the glovebox. The scan rate is 80 mV s<sup>-1</sup> and scanning range is -0.04–0.9 V. The light intensity was adjusted from 1 to 100 mW cm<sup>-2</sup> to perform the light intensity dependence tests. The corresponding measured area of

devices defined with a non-reflective black shadow mask is 0.0576 cm<sup>2</sup>. The solar cell quantum efficiency measurement system (QE-R, Enlitech) was employed to obtain the spectral response of different PSCs and TSCs. Mott-Schottky plots and EIS measurements were performed using the all-in-one characterization system (PAIOS, Fluxim AG). External electroluminescence quantum efficiency (EQE<sub>EL</sub>) measurement was measured on ELCT-3010 (Enlitech) with a step of 0.1 V. The MPP tracking was performed using multicolor LED solar simulator (Guangzhou Crysco Equipment Co. Ltd) with AM1.5 G, 100 mW cm<sup>-2</sup> in the glovebox at about 25–30 °C.

### Reporting summary

Further information on research design is available in the Nature Portfolio Reporting Summary linked to this article.

### Data availability

All the main data are available in the main text, the Supplementary Information, and the Source Data file. All other data of this study are available from the corresponding authors on request. Source data are provided with this paper.

### References

- Green, M. A. et al. Solar cell efficiency tables. *Prog. Photovolt. Res. Appl.* **32**, 425–441 (2024).
- Leijtens, T., Bush, K. A., Prasanna, R. & McGehee, M. D. Opportunities and challenges for tandem solar cells using metal halide perovskite semiconductors. *Nat. Energy* **3**, 828–838 (2018).
- Anaya, M., Lozano, G., Calvo, M. E. & Míguez, H. ABX<sub>3</sub> perovskites for tandem solar cells. *Joule* **1**, 769–793 (2017).
- Zhu, J. & Zhao, D. All-perovskite tandem solar cells gallop ahead. *Innovation* **4**, 100493 (2023).
- Zhao, D. et al. Efficient two-terminal all-perovskite tandem solar cells enabled by high-quality low-bandgap absorber layers. *Nat. Energy* **3**, 1093–1100 (2018).
- Zhao, D. et al. Low-bandgap mixed tin-lead iodide perovskite absorbers with long carrier lifetimes for all-perovskite tandem solar cells. *Nat. Energy* **2**, 17018 (2017).
- Gao, H. et al. Homogeneous crystallization and buried interface passivation for perovskite tandem solar modules. *Science* **383**, 855–859 (2024).
- Lin, R. et al. Monolithic all-perovskite tandem solar cells with 24.8% efficiency exploiting comproportionation to suppress Sn(II) oxidation in precursor ink. *Nat. Energy* **4**, 864–873 (2019).
- Tong, J. et al. Carrier lifetimes of >1 us in Sn-Pb perovskites enable efficient all-perovskite tandem solar cells. *Science* **364**, 475–479 (2019).
- Lin, R. et al. All-perovskite tandem solar cells with improved grain surface passivation. *Nature* **603**, 73–78 (2022).
- Zhou, S. et al. Aspartate all-in-one doping strategy enables efficient all-perovskite tandems. *Nature* **624**, 69–73 (2023).
- Chen, H. et al. Regulating surface potential maximizes voltage in all-perovskite tandems. *Nature* **613**, 676–681 (2023).
- Wang, C. et al. A universal close-space annealing strategy towards high-quality perovskite absorbers enabling efficient all-perovskite tandem solar cells. *Nat. Energy* **7**, 744–775 (2022).
- Wang, J. et al. Bimolecular crystallization modulation boosts the efficiency and stability of Methylammonium-free tin-lead perovskite and all-perovskite tandem solar cells. *Adv. Energy Mater.* **14**, 2402171 (2024).
- Yu, Z. et al. Simplified interconnection structure based on  $C_{60}/SnO_{2-x}$  for all-perovskite tandem solar cells. *Nat. Energy* **5**, 657–665 (2020).
- Jiang, Q. et al. Compositional texture engineering for highly stable wide-bandgap perovskite solar cells. *Science* **378**, 1295–1300 (2022).
- Jiang, F. et al. A two-terminal perovskite/perovskite tandem solar cell. *J. Mater. Chem. A* **4**, 1208–1213 (2016).

18. Lin, R. et al. All-perovskite tandem solar cells with 3D/3D bilayer perovskite heterojunction. *Nature* **620**, 994–1000 (2023).
19. Liu, C. et al. Efficient all-perovskite tandem solar cells with low-optical-loss carbazoyl interconnecting layers. *Angew. Chem. Int. Ed.* **62**, e202313374 (2023).
20. Li, C. et al. Diamine chelates for increased stability in mixed Sn-Pb and all-perovskite tandem solar cells. *Nat. Energy* <https://doi.org/10.1038/s41560-024-01613-8> (2024).
21. Al-Ashouri, A. et al. Conformal monolayer contacts with lossless interfaces for perovskite single junction and monolithic tandem solar cells. *Energy Environ. Sci.* **12**, 3356–3369 (2019).
22. Tan, Q. et al. Inverted perovskite solar cells using dimethylacridine-based dopants. *Nature* **620**, 545–551 (2023).
23. Yi, Z. et al. Achieving a high open-circuit voltage of 1.339 V in 1.77-eV wide-bandgap perovskite solar cells via self-assembled monolayers. *Energy Environ. Sci.* **17**, 202–209 (2023).
24. Jiang, W. et al.  $\pi$ -Expanded carbazoles as hole-selective self-assembled monolayers for high-performance perovskite solar cells. *Angew. Chem. Int. Ed.* **61**, e202213560 (2022).
25. Liu, M. et al. Defect-passivating and stable benzothiophene-based self-assembled monolayer for high-performance inverted perovskite solar cells. *Adv. Energy Mater.* **14**, 2303742 (2024).
26. Park, S. M. et al. Low-loss contacts on textured substrates for inverted perovskite solar cells. *Nature* **624**, 289–294 (2023).
27. Tang, H. et al. Reinforcing self-assembly of hole transport molecules for stable inverted perovskite solar cells. *Science* **383**, 1236–1240 (2024).
28. Tong, X. et al. Large orientation angle buried substrate enables efficient flexible perovskite solar cells and modules. *Adv. Mater.* **36**, 2407032 (2024).
29. Liu, S. et al. Triple-junction solar cells with cyanate in ultrawide-bandgap perovskites. *Nature* **628**, 306–312 (2024).
30. Qu, G. et al. Conjugated linker-boosted self-assembled monolayer molecule for inverted perovskite solar cells. *Joule* **8**, 2123–2134 (2024).
31. Li, M., Liu, M., Qi, F., Lin, F. R. & Jen, A. K. Y. Self-assembled monolayers for interfacial engineering in solution-processed thin-film electronic devices: design, fabrication, and applications. *Chem. Rev.* **124**, 2138–2204 (2024).
32. Li, C. et al. Pros and cons of hole-selective self-assembled monolayers in inverted PSCs and TSCs: extensive case studies and data analysis. *Energy Environ. Sci.* **17**, 6157–6203 (2024).
33. Xu, D., Wu, P. & Tan, H. Self-assembled monolayers for perovskite solar cells. *Inf. Funct. Mater.* **1**, 2–25 (2024).
34. Wang, Y. et al. Teaching an old anchoring group new tricks: enabling low-cost, eco-friendly hole-transporting materials for efficient and stable perovskite solar cells. *J. Am. Chem. Soc.* **142**, 16632–1664 (2020).
35. Magomedov, A. et al. Self-assembled hole transporting monolayer for highly efficient perovskite solar cells. *Adv. Energy Mater.* **8**, 201801892 (2018).
36. Aydin, E. et al. Enhanced optoelectronic coupling for perovskite/silicon tandem solar cells. *Nature* **623**, 732–738 (2023).
37. Li, L. et al. Flexible all-perovskite tandem solar cells approaching 25% efficiency with molecule-bridged hole-selective contact. *Nat. Energy* **7**, 708–717 (2022).
38. He, R. et al. All-perovskite tandem 1 cm<sup>2</sup> cells with improved interface quality. *Nature* **618**, 80–86 (2023).
39. Wang, Z. et al. Suppressed phase segregation for triple-junction perovskite solar cells. *Nature* **618**, 74–79 (2023).
40. Chin, Y.-C., Daboczi, M., Henderson, C., Luke, J. & Kim, J.-S. Suppressing PEDOT:PSS doping-induced interfacial recombination loss in perovskite solar cells. *ACS Energy Lett.* **7**, 560–56 (2022).
41. Chen, L. et al. Incorporating potassium citrate to improve the performance of tin-lead perovskite solar cells. *Adv. Energy Mater.* **13**, 2301218 (2023).
42. Zhou, J. et al. Acidity control of interface for improving stability of all-perovskite tandem solar cells. *Adv. Energy Mater.* **13**, 2300968 (2023).
43. Fu, S. et al. Suppressed deprotonation enables a durable buried interface in tin-lead perovskite for all-perovskite tandem solar cells. *Joule* **8**, 2220–2237 (2024).
44. Yu, Z. et al. Solution-processed ternary tin (II) alloy as hole-transport layer of Sn-Pb perovskite solar cells for enhanced efficiency and stability. *Adv. Mater.* **34**, 2205769 (2022).
45. Bai, Y. et al. Decoupling light- and oxygen-induced degradation mechanisms of Sn-Pb perovskites in all perovskite tandem solar cells. *Energy Environ. Sci.* **17**, 8557–8569 (2024).
46. Wang, J. et al. Enhancing photostability of Sn-Pb perovskite solar cells by an alkylammonium pseudo-halogen additive. *Adv. Energy Mater.* **13**, 2204115 (2023).
47. Zhu, J. et al. Custom-tailored hole transport layer using oxalic acid for high-quality tin-lead perovskites and efficient all-perovskite tandems. *Sci. Adv.* **10**, adL2063 (2024).
48. Zhu, J. et al. A donor-acceptor-type hole-selective contact reducing non-radiative recombination losses in both subcells towards efficient all-perovskite tandems. *Nat. Energy* **8**, 714–724 (2023).
49. Zhang, Z. et al. Anchoring charge selective self-assembled monolayers for tin-lead perovskite solar cells. *Adv. Mater.* **36**, 2312264 (2024).
50. Kappel, G. et al. Tin-lead perovskite solar cells fabricated on hole selective monolayers. *ACS Energy Lett.* **7**, 966–974 (2022).
51. Pitaro, M. et al. Tuning the surface energy of hole transport layers based on carbazole self-assembled monolayers for highly efficient Sn/Pb perovskite solar cells. *Adv. Funct. Mater.* **34**, 2306571 (2023).
52. Hu, S. et al. Optimized carrier extraction at interfaces for 23.6% efficient tin-lead perovskite solar cells. *Energy Environ. Sci.* **15**, 2096–2107 (2022).
53. Zhou, J. et al. Mixed tin-lead perovskites with balanced crystallization and oxidation barrier for all-perovskite tandem solar cells. *Nat. Commun.* **15**, 2324 (2024).
54. Hu, S. et al. Narrow bandgap metal halide perovskites for all-perovskite tandem photovoltaics. *Chem. Rev.* **124**, 4079–4123 (2024).
55. Zhou, Y. et al. Interfacial modification of NiO<sub>x</sub> for highly efficient and stable inverted perovskite solar cells. *Adv. Energy Mater.* **14**, 2400616 (2024).
56. Luo, Y. et al. Enhanced efficiency and stability of wide-bandgap perovskite solar cells via molecular modification with piperazinium salt. *Adv. Energy Mater.* **14**, 2304429 (2024).
57. Liao, Q. et al. Self-assembled donor-acceptor hole contacts for inverted perovskite solar cells with an efficiency approaching 22%: the impact of anchoring groups. *J. Energy Chem.* **68**, 87–95 (2022).
58. Cheng, Q. et al. Molecular self-assembly regulated dopant-free hole transport materials for efficient and stable n-i-p perovskite solar cells and scalable modules. *Angew. Chem. Int. Ed.* **61**, e2210613 (2022).
59. Zhou, H. et al. Glycol monomethyl ether-substituted carbazoyl hole-transporting material for stable inverted perovskite solar cells with efficiency of 25.52%. *Angew. Chem. Int. Ed.* **63**, e202403068 (2024).
60. Yu, Z. et al. Intramolecular electric field construction in metal phthalocyanine as dopant-free hole transporting material for stable perovskite solar cells with >21% efficiency. *Angew. Chem. Int. Ed.* **60**, 6294–6299 (2021).
61. Lee, J., Kim, G. W., Kim, M., Park, S. A. & Park, T. Nonaromatic green-solvent-processable, dopant-free, and lead-capturable hole transport polymers in perovskite solar cells with high efficiency. *Adv. Energy Mater.* **10**, 1902662 (2020).
62. Wang, H. et al. Interface dipole management of D-A-type molecules for efficient perovskite solar cells. *Angew. Chem. Int. Ed.* **63**, e202404289 (2024).

63. Ma, Y., Gong, J., Zeng, P. & Liu, M. Recent progress in interfacial dipole engineering for perovskite solar cells. *Nano-Micro Lett.* **15**, 173 (2023).
64. Zhao, S. et al. Cross-plane transport in a single-molecule two-dimensional van der Waals heterojunction. *Sci. Adv.* **6**, eaba6714 (2020).
65. Wang, X. et al. Regulating phase homogeneity by self-assembled molecules for enhanced efficiency and stability of inverted perovskite solar cells. *Nat. Photo.* <https://doi.org/10.1038/s41566-024-01531-x> (2024).
66. Liu, S. et al. Buried interface molecular hybrid for inverted perovskite solar cells. *Nature* **632**, 536–542 (2024).
67. Warby, J. et al. Mismatch of quasi-fermi level splitting and  $V_{OC}$  in perovskite solar cells. *Adv. Energy Mater.* **13**, 202303135 (2023).
68. Latypova, A. F. et al. Design principles for organic small molecule hole-transport materials for perovskite solar cells: Film morphology matters. *ACS Appl. Energy Mater.* **5**, 5395–5403 (2022).
69. Jiang, X. et al. Ultra-high open-circuit voltage of tin perovskite solar cells via an electron transporting layer design. *Nat. Commun.* **11**, 1245 (2020).
70. Sun, X. et al. Multifunctional modification of the buried interface in mixed tin-lead perovskite solar cells. *Angew. Chem., Int. Ed.* **63**, e202409330 (2024).
71. Wang, J. et al. Highly efficient all-inorganic perovskite solar cells with suppressed non-radiative recombination by a Lewis base. *Nat. Commun.* **11**, 177 (2020).
72. Wei, K. et al. Facile exfoliation of the perovskite thin film for visualizing the buried interfaces in perovskite solar cells. *ACS Appl. Energy Mater.* **5**, 7458–7465 (2022).
- sectional SEM measurements of all-perovskite TSCs. Y.X., Z.G. and J. Zhu performed EQE of LBG and WBG PSCs. T.M. helped to performed MPP tracking of tandems. K.W. and J. Zhang performed the exfoliation of perovskite films and characterized the PL mapping and SEM of the buried interface. Z.Z., W.L. and S.R. helped to performed XRD patterns. J. Zhu, Y.W. and D.Z. wrote the manuscript with inputs from all co-authors. All authors discussed the results and reviewed the manuscript. D.Z. directed this project.

### Competing interests

The authors declare no competing interests.

### Additional information

**Supplementary information** The online version contains supplementary material available at <https://doi.org/10.1038/s41467-024-55492-4>.

**Correspondence** and requests for materials should be addressed to Yang Wang, Cong Chen, Jinbao Zhang or Dewei Zhao.

**Peer review information** *Nature Communications* thanks Zhike Liu, Bowen Yang and the other, anonymous, reviewer(s) for their contribution to the peer review of this work. A peer review file is available.

**Reprints and permissions information** is available at <http://www.nature.com/reprints>

**Publisher's note** Springer Nature remains neutral with regard to jurisdictional claims in published maps and institutional affiliations.

**Open Access** This article is licensed under a Creative Commons Attribution-NonCommercial-NoDerivatives 4.0 International License, which permits any non-commercial use, sharing, distribution and reproduction in any medium or format, as long as you give appropriate credit to the original author(s) and the source, provide a link to the Creative Commons licence, and indicate if you modified the licensed material. You do not have permission under this licence to share adapted material derived from this article or parts of it. The images or other third party material in this article are included in the article's Creative Commons licence, unless indicated otherwise in a credit line to the material. If material is not included in the article's Creative Commons licence and your intended use is not permitted by statutory regulation or exceeds the permitted use, you will need to obtain permission directly from the copyright holder. To view a copy of this licence, visit <http://creativecommons.org/licenses/by-nc-nd/4.0/>.

© The Author(s) 2025

### Acknowledgements

This work was financially supported by the National Key R&D Program of China (no. 2022YFB4200303 to D.Z.), the National Natural Science Foundation of China (nos. 62174112 to D.Z. and 22379126 to J.Zhang), the Fundamental Research Funds for the Central Universities (no. YJ2021157 to C.C.), the Engineering Featured Team Fund of Sichuan University (no. 2020SCJUN102 to D.Z.), and the Natural Science Foundation Project of Fujian Province (no. 2023J01527 to Y.W.).

### Author contributions

D.Z., Y.W. and J. Zhu conceived and designed the research. J. Zhu carried out the fabrication and characterization of LBG PSCs and all-perovskite TSCs. X.H. and Y.W. synthesized the SCMs and provide the relevant characterizations of SCMs. J. Zhu, Y.L., J.W. and Y.X. fabricated 2-T all-perovskite tandems. J. Zhu, W.J. and Z.G. fabricated 4-T all-perovskite tandems. Y.X., J.Y. and J.J. helped to optimize the LBG devices. Y.L., J.W., Z.G., S.W., W.J. and C.C. helped to optimize the WBG devices. T.M., J. Zhu and C.W. performed EQE and cross-